NANO LETTERS
Letter
pubs.acs.org/NanoLett

Tailoring the Optical Characteristics of Microsized InP Nanoneedles Directly Grown on Silicon

Kun Li,[†] Hao Sun,[†,‡] Fan Ren,[†] Kar Wei Ng,[†] Thai-Truong D. Tran,[†] Roger Chen,[†]
and Connie J. Chang-Hasnain*,[†]

[†]Department of Electrical Engineering and Computer Sciences, University of California at Berkeley, Berkeley, California 94720, United States

[‡]Department of Electronic Engineering, Tsinghua University, Beijing 100084, P. R. China

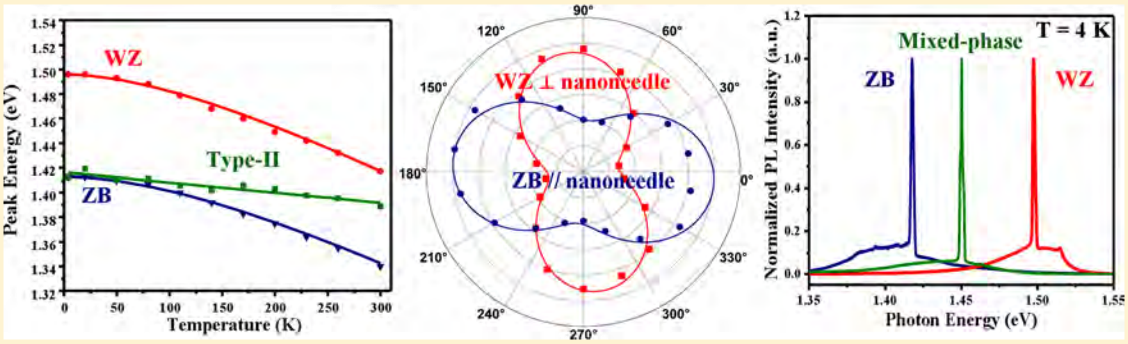

ABSTRACT: Nanoscale self-assembly offers a pathway to realize heterogeneous integration of III−V materials on silicon. However, for III−V nanowires directly grown on silicon, dislocation-free single-crystal quality could only be attained below certain critical dimensions. We recently reported a new approach that overcomes this size constraint, demonstrating the growth of single-crystal InGaAs/GaAs and InP nanoneedles with the base diameters exceeding 1 μm. Here, we report distinct optical characteristics of InP nanoneedles which are varied from mostly zincblende, zincblende/wurtzite-mixed, to pure wurtzite crystalline phase. We achieved, for the first time, pure single-crystal wurtzite-phase InP nanoneedles grown on silicon with bandgaps of 80 meV larger than that of zincblende-phase InP. Being able to attain excellent material quality while scaling up in size promises outstanding device performance of these nanoneedles. At room temperature, a high internal quantum efficiency of 25% and optically pumped lasing are demonstrated for single nanoneedle as-grown on silicon substrate. Recombination dynamics proves the excellent surface quality of the InP nanoneedles, which paves the way toward achieving multijunction photovoltaic cells, long-wavelength heterostructure lasers, and advanced photonic integrated circuits.

KEYWORDS: *InP nanowire, silicon, type-II, wurtzite, photovoltaics, nanolaser*

Silicon is the backbone of modern electronic technology, which enabled the manipulation of electrons for a variety of innovative purposes. Coaxing silicon to manipulate photons, in contrast, is much more difficult. One of the key goals of optoelectronics is therefore to integrate materials with superior optical properties, such as III−V semiconductors, onto a silicon platform, combining the strengths of both materials. However, fundamental incompatibilities, such as mismatches of crystal lattices and synthesis temperatures, prevent the epitaxial growth of III−V on silicon. Self-assembly of nanstructures, such as nanowires, opens a pathway to accommodate lattice-mismatch. Semiconductor nanowires show promise in several diverse application areas, such as electronics, sensor technology, and biosciences. Synthesis of nanowires with a variety of materials has been demonstrated, among which GaAs and InP-based III−V materials are typically used for optoelectronic applications.[1] Growth of GaAs and InP-based nanowires on native substrate has led to remarkable results,[2,3] while heterogeneous growth on silicon still remains highly challenging. A few attempts were made toward heterogeneous growth, either with gold catalyst[4] or at high temperature,[5,6] which are considered incompatible with complementary metal−oxide−semiconductor (CMOS) device manufacturing.[7,8] More importantly, these growth techniques cannot surmount the size constraint of nanowires, which are limited to a few hundreds of nanometers in diameter.[9] We demonstrated catalyst-free low-temperature growth of single-crystal InGaAs/GaAs nanoneedles on silicon with base diameters far beyond critical dimensions.[7,10] The advantages have been shown with various optoelectronic devices reported.[11,12] The development of InP nanoneedles self-assembled by the same growth mode on silicon has been carried on recently.[13] Among the family of III−V compounds, InP is less susceptible to recombination at free surfaces.[14] A low surface recombination velocity (and therefore high internal

Received: October 4, 2013
Revised: November 26, 2013
Published: December 3, 2013

quantum efficiency (IQE)) makes InP an excellent candidate for devices. Moreover, as a growth template for many other compound semiconductors, InP monolithically grown on silicon is also potentially useful as a means to achieving multijunction photovoltaic cells, as well as long-wavelength heterostructure nanolasers with silicon-transparent emission.[13]

Early investigations of semiconductor nanowires were marked by a number of surprise discoveries, including the finding that nanostructured wires often adopt a hexagonal wurtzite (WZ) crystal phase with a different band structure from the cubic zincblende (ZB) phase existing in bulk form.[15,16] However, twinning and ZB/WZ-mixed polytypism have been a well-known issue for InP nanowires. This poses a challenge to achieving a pure crystalline phase. The mixed-phase crystal in nanowires has a major impact on the nanowires' optical properties and device performance due to electron scattering at stacking faults or twin planes.[17] Extensive studies have been devoted to the crystal phase transition of InP nanowires grown natively on an InP substrate.[18,19] However, none of these studies have covered a complete optical characterization up to room temperature, mainly restricted by limited optical luminescence yield.

In this paper, we demonstrate the extraordinary capabilities of InP nanoneedles as-grown on silicon for multiple optoelectronic applications in three aspects. (1) We tailor the optical characteristics of InP nanoneedles through crystal phase transition, by tuning growth temperature from 400 to 450 °C. Dislocation-free single-crystal WZ-phase InP nanoneedles with base diameters beyond 1 μm were demonstrated. Optical properties of InP nanoneedles in different crystal phases are studied comprehensively up to room temperature, for the first time, exploiting the high optical luminescence yield due to bigger size. (2) Recombination dynamics characterization indicates excellent surface quality of InP nanoneedles, which is critical for future development of heterostructure devices. A larger bandgap and higher IQE make WZ-phase InP nanoneedles stand out for photovoltaics. (3) Each nanoneedle provides a natural optical cavity, with optically pumped laser demonstrated up to room temperature. This predicts a direction for on-chip laser sources in the optical communication domain.

InP nanoneedles were grown on a surface-roughened silicon (111) substrate using low-temperature metal−organic chemical vapor deposition (MOCVD) in a catalyst-free environment. The nanoneedles were verified to be core−shell structures with dimensions that can be scaled up in direct proportion to the growth time.[13] A range of growth temperatures were explored (400−450 °C), and samples grown at two temperatures were found to be of particular interest (labeled "sample A" and "sample B" in what follows). Sample A, grown at 425 °C, consists of very long needles with a taper angle of approximately 3°, as seen in Figure 1a. Sample B, grown at a higher temperature of 450 °C, features shorter nanoneedles with a taper angle of about 8° (Figure 1b). Both needle types have a clearly faceted hexagonal cross-section. It is worth noting that the base diameters of these nanoneedles are both around 0.8 μm, far beyond the lattice-mismatch critical dimension (around 40 nm).[9] A longer growth time yielded nanoneedles with diameters above 1 μm (up to 1.4 μm demonstrated), which are not shown here.

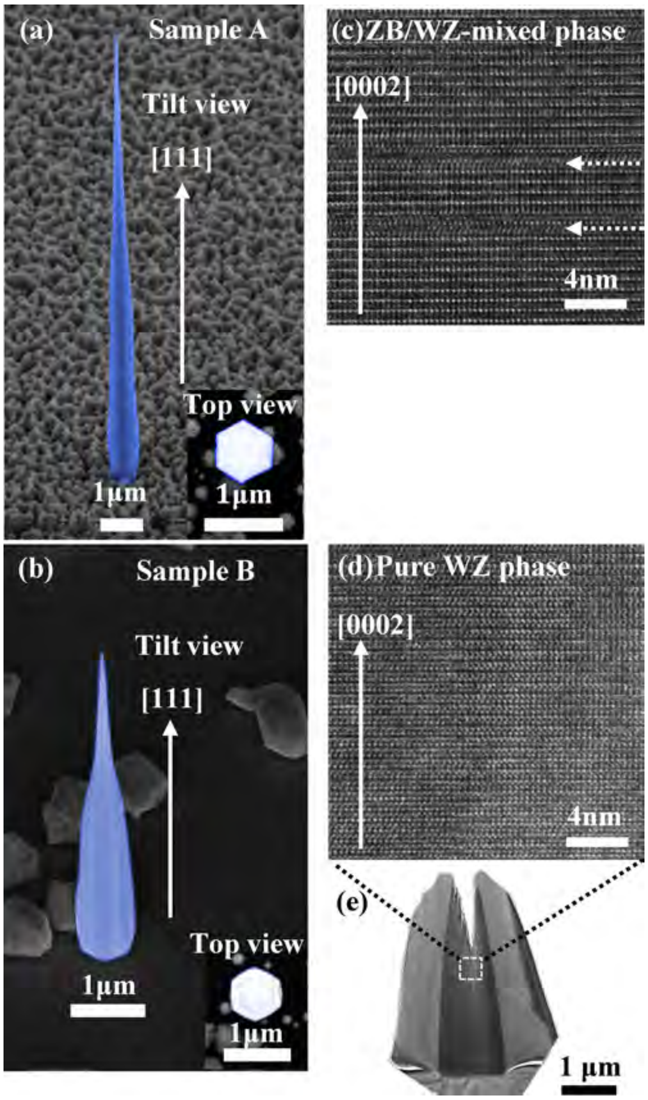

Figure 1. InP nanoneedle structure and phase composition. Sample A: ZB/WZ-mixed polytypic crystal phase. Sample B: pure WZ crystal phase. (a) 45° tilt view and top view (inset) of a typical mixed-phase nanoneedle from sample A, as seen by scanning electron microscopy (SEM). The images reveal a needle with a sharp tip (3° taper angle), hexagonal cross-section, diameter of 0.8 μm, and height of 15.2 μm. (b) 45° tilt view and top view (inset) SEM images of a typical WZ-phase nanoneedle from sample B. The images reveal a needle with a sharp tip (8° taper angle), hexagonal cross-section, diameter of 0.8 μm and height of 5.8 μm. (c) HRTEM image of a typical nanoneedle from sample A, exhibiting ZB/WZ-mixed polytypic crystal phase. Dashed arrows indicate two major stacking faults in this region, caused by the ZB phase mixed in the WZ phase. (d) HRTEM image of a typical nanoneedle from sample B, in pure single-crystal WZ phase. (e) Bright-field TEM image of a thin lamella cut from the center of a WZ-phase nanoneedle with FIB. The dashed box highlights the area in the major body part from where the zoomed-in HRTEM image of d is taken.

High-resolution transmission electron microscopy (HRTEM) was used to study the structural composition of the InP nanoneedles. With the use of focused ion beam (FIB) and micromanipulator, we cut across the center of the nanoneedle and transferred the thin slice, or lamella, to a liftout grid. The lamella was then further thinned down to electron transparent thickness with an argon ion beam. HRTEM images and diffraction patterns were obtained from the thin lamella. More details on the method are described in ref 10. Nanoneedles from sample A consist of a ZB/WZ-mixed

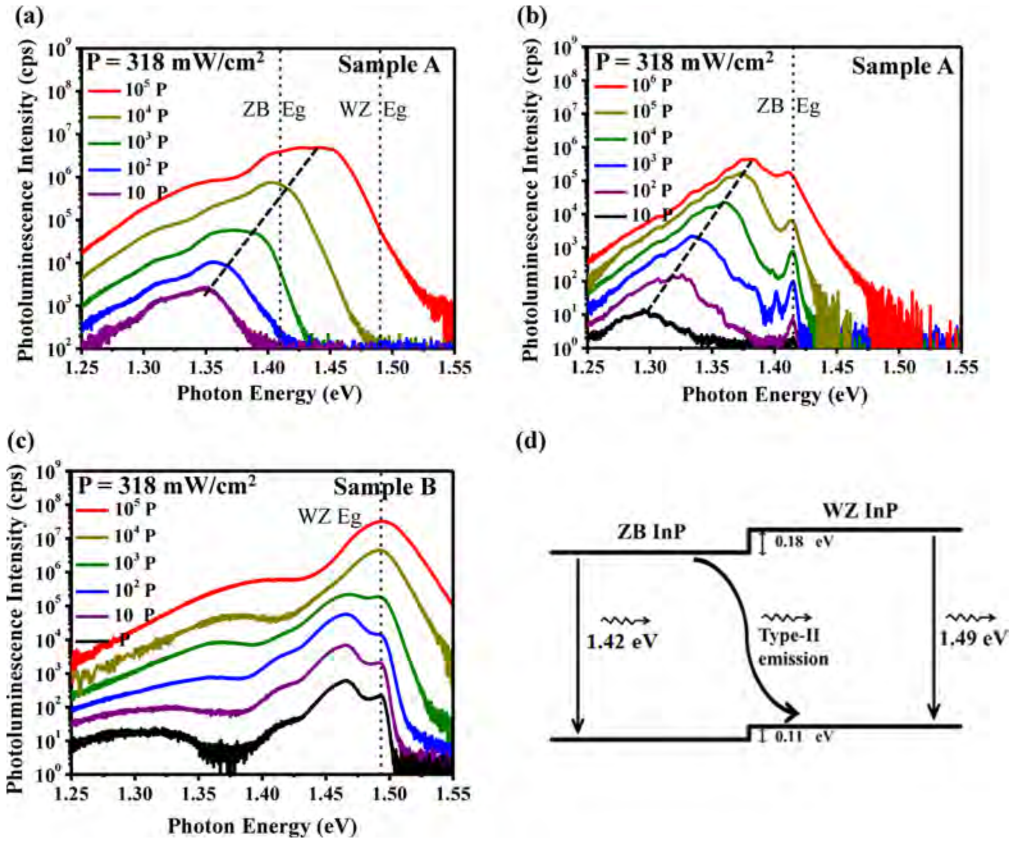

Figure 2. PL spectra at 4 K under a range of laser pump powers (660-nm CW diode laser, power density from P to 10^5 P, with P = 318 mW/cm^2). (a) A typical mixed-phase nanoneedle from sample A, displaying type-II emission with a significant blue-shift of 27.7 meV per decade, from 1.35 to 1.45 eV. (b) A mostly-ZB-phase nanoneedle from sample A that exhibits a ZB band-edge emission peak at 1.41 eV in addition to the type-II emission peak. (c) A typical WZ-phase nanoneedle, showing WZ band-edge emission at 1.49 eV and defect emission at 1.45 eV. (d) Band structure of ZB/WZ InP heterojunction at 0 K; WZ-phase InP has a larger bandgap and valence band offset of 0.11 eV compared with ZB-phase InP. The three carrier recombination paths (ZB band-edge, WZ band-edge, and type-II indirect recombination) are illustrated.

polytypic crystal phase (referred as “mixed-phase nanoneedles”), as shown in Figure 1c. Nanoneedles from sample B are made up of essentially pure WZ crystal phase (referred as “WZ-phase nanoneedles”), with minimal stacking faults mostly confined to the root region and terminated at the sidewalls, benefitting from the core−shell growth mode (Figure 1d). In Figure 1e, a bright-field TEM image of the WZ-phase nanoneedle lamella is displayed, highlighting the major body area corresponding to the zoomed-in HRTEM image in Figure 1d.

Microphotoluminescence (μ-PL) measurements were done by delivering continuous-wave (CW) excitation from a 660 nm diode laser to individual InP nanoneedles as-grown on a silicon substrate (see ref 7 for more details). Results shown here are all from typical nanoneedles that can represent the average performance of all nanoneedles on the same sample in terms of PL spectrum and intensity. For the typical mixed-phase nanoneedles from sample A, we observed a significant blue-shift in the PL spectrum with increasing pump power at 4 K. As shown in Figure 2a, the PL emission peak shifts from 1.35 to 1.45 eV, at a rate of about 27.7 meV per 10 times of pump power increase (per decade). In addition, a smaller portion of nanoneedles from sample A (Figure 2b) exhibits a second emission peak around 1.41 eV, which matches the bandgap (E_g ∼ 1.41−1.42 eV) of the ZB-phase InP (referred as “ZB-emission”). For WZ-phase nanoneedles (sample B), the PL spectrum consists of two peaks—a WZ-phase band-edge emission at 1.49 eV (referred as “WZ-emission”) and an emission peak at 1.45 eV that saturates rapidly with increasing pump power (Figure 2c). The fact that the peak at 1.45 eV was observed at nearly the same energy for thousands of nanoneedles tested suggests that the recombination involves bulk-related states, such as carbon-induced impurities[14] or radiative defects.[20] In contrast to mixed-phase nanoneedles, WZ-phase nanoneedles did not exhibit an observable blue-shift for either the 1.49 eV WZ-emission peak or the 1.45 eV emission peak (referred as “defect-emission”).

Figure 2d illustrates the band structure for ZB/WZ InP heterojunction at 0 K, reconstructed from theoretical calculations.[16] A larger bandgap of 1.49 eV and a valence band offset of 0.11 eV are found in the pure WZ crystal phase of InP as compared to pure ZB-phase InP. The alternating of these two crystal phases within a given nanoneedle sample will generally introduce a type-II band alignment, whereby electrons are confined to ZB-phase segments and holes are confined to WZ-phase segments. The space charge due to carrier separation then induces an electric field across the heterojunction between the ZB and WZ segments, which brings about band bending at the interface, thus generating a triangular potential well with quantized energy levels.[21] Under a higher pump power, more carrier charges accumulate at the interface, thus enhancing the band-bending. The effective potential well width is then reduced so as to raise energy levels, causing a blue-shift in the PL emission as pump power increases. This blue-shift is

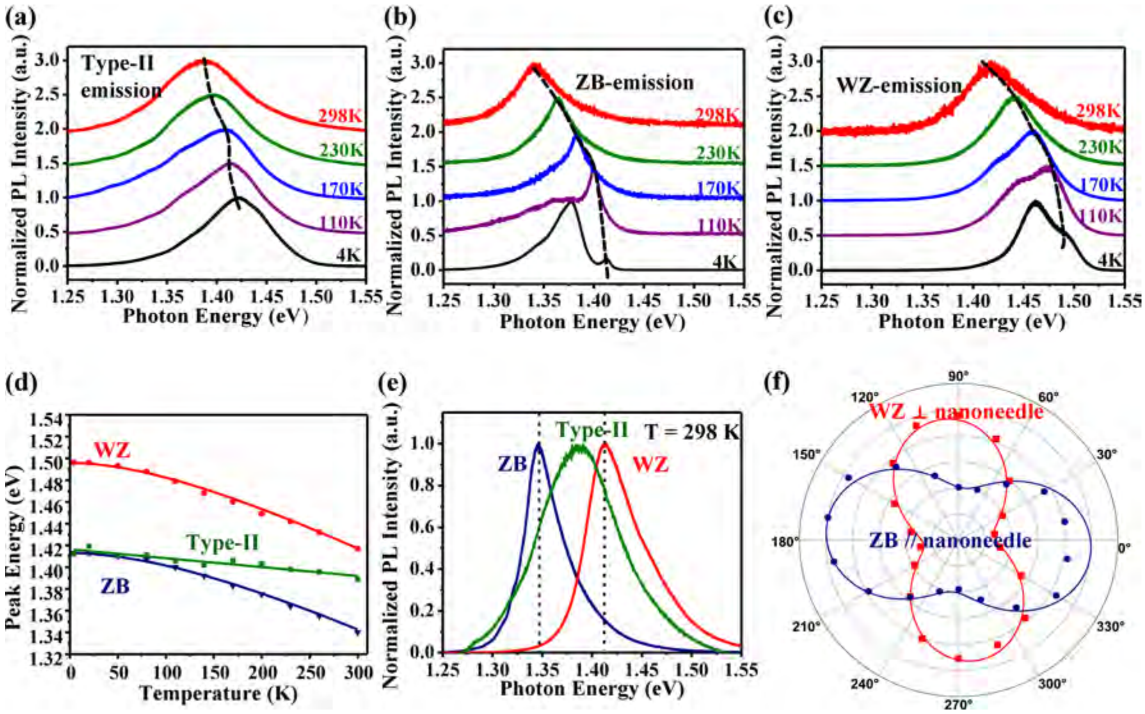

Figure 3. Temperature-dependent and polarization-dependent PL spectra of InP nanoneedles. Temperature ranges from 4 to 298 K; the nanoneedles are pumped by a 660 nm CW diode laser at an excitation power density of 2×10^4 P (P = 318 mW/cm^2). (a) Typical mixed-phase nanoneedle. (b) Mostly-ZB-phase nanoneedle. (c) Typical WZ-phase nanoneedle. (d) PL emission peak energy as a function of temperature for the three needle categories in a−c. The dark blue curve corresponds to ZB-emission in b, fitted with the Varshni equation (see text for details). The red curve corresponds to WZ-emission in c, fitted with a modified Varshni equation (see text for details). The green curve corresponds to type-II emission in a. (e) Room-temperature PL spectra for the three types of nanoneedles, showing emission peaks at 1.34 eV (dark blue, ZB-emission), 1.41 eV (red, WZ-emission), and 1.39 eV (green, type-II emission). (f) Polarization dependence of the integrated PL intensity for ZB-emission (dark blue) and WZ-emission (red), with the solid line indicating a fit to $\sin^2\theta$. The radial scale lines represent normalized PL intensity, while the tangential scale lines represent polarization angle with respect to the nanoneedle axis.

usually regarded as experimental evidence for type-II band structure.[22,23] As such, we conclude that the significant blue-shifts observed in the PL spectra of mixed-phase nanoneedles originate from the prevailing type-II band structure. The observation of ZB emission from some of the nanoneedles on sample A (Figure 2b) is likely due to the formation of more ZB phase induced by fluctuations in local growth conditions across the sample wafer.[19] We call such needles as "mostly-ZB-phase nanoneedles" in the following context.

To further shed light on the origin of the PL for each type of nanoneedle, temperature-dependent CW-PL measurements were performed (Figure 3a−c). The temperature was varied from 4 to 298 K using a continuous-flow liquid-helium cryostat. The temperature evolution of the PL spectrum for the mostly-ZB-phase nanoneedle (Figure 2b) is illustrated in Figure 3b. The type-II peak gradually saturates with increasing temperature until about 110 K, above which only the ZB-emission peak remains. The ZB-emission peak energy is shown as a function of measurement temperature (T) by the dark blue curve in Figure 3d, which can be fitted very well with the Varshni equation $E_g = 1.413 - 4.9 \times 10^{-4}\ T^2/(T + 327)$, revealing a bandgap of 1.413 eV at 0 K.[24,25] For WZ-phase nanoneedles, the defect-emission peak saturates as temperature rises, while WZ-emission is preserved (Figure 3c). The WZ-emission peak energy, shown as a function of temperature by the red curve in Figure 3d, can also be fitted well using a slightly modified Varshni equation: $E_g = 1.496 - 4.9 \times 10^{-4}\ T^2/(T + 260)$, revealing a bandgap of 1.496 eV at 0 K.[24−26] Intriguingly, a typical mixed-phase nanoneedle (Figures 2a and 3a) exhibits type-II emission all the way up to 298 K, with peak energy fluctuating (green curve in Figure 3d). However, we no longer observe blue-shift behavior with increasing pump power above 110 K, partly due to a broadened PL spectrum at higher temperature. Figure 3e shows the normalized PL spectra for the three types of nanoneedles at room temperature. As far as we know, this is the first thorough analysis of the emission spectra of InP nanostructures as the crystal phase and temperature vary.

Distinctive differences between the optical properties of the different InP crystal phases can also be seen by studying the polarization of the ZB emission and WZ emission (shown in Figure 3e) at 298 K. The as-grown nanoneedles were mechanically removed and placed horizontally onto a carrier substrate. Polarization measurement was performed by inserting a linear polarizer into the PL signal collection path and tuning the polarization angle. As seen in Figure 3f, the ZB emission is strongly (74%) polarized parallel to the nanoneedle axis, due to the dielectric contrast between the higher-index nanoneedle bulk and the surrounding air. In contrast, the WZ emission is strongly (78%) polarized perpendicular to the nanoneedle axis, because the hexagonal WZ-phase crystal undergoes valence band splitting.[26]

The IQE of a system is intimately linked to the carrier recombination lifetime and is an important figure of merit for optoelectronic devices such as photovoltaic cells. To elucidate the carrier recombination lifetime of our InP nanoneedles, we studied the recombination dynamics of both mixed-phase nanoneedles and WZ-phase nanoneedles using time-resolved photoluminescence (TRPL) measurements. Time correlated

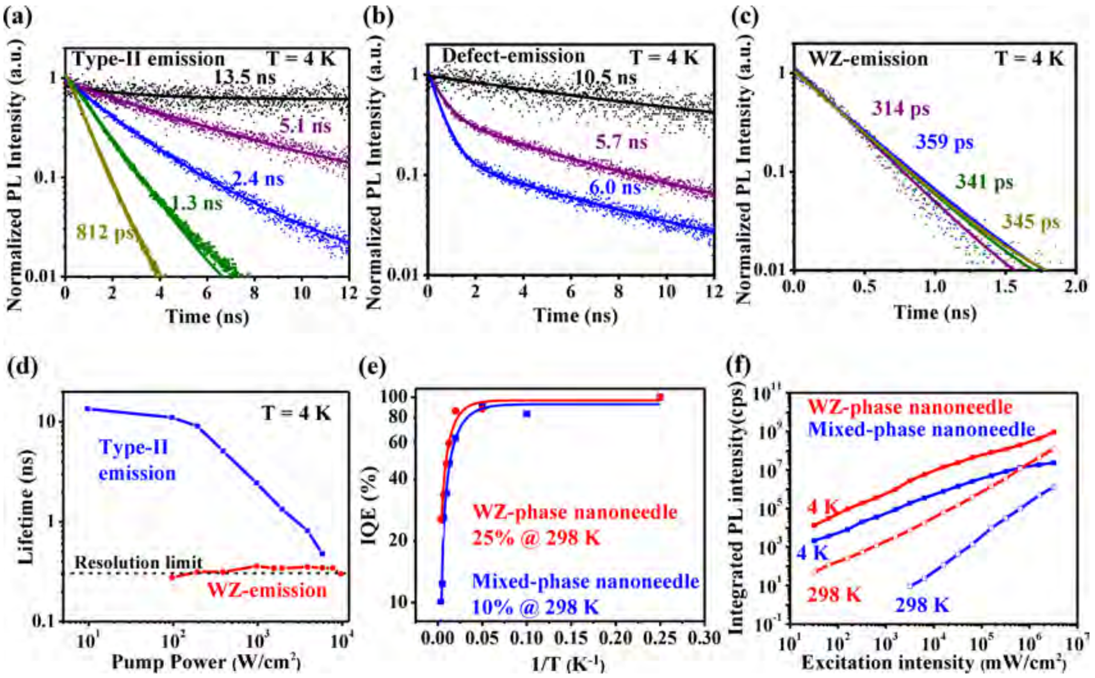

Figure 4. Recombination dynamics and IQE. TRPL data (dots) measured using the TCSPC method, pumped by a titanium−sapphire fs laser at 750 nm. The data are fitted with an exponential decay function (solid curves). (a) Type-II emission from typical mixed-phase nanoneedles with increasing pump power. The carrier lifetime is 13.5 ns at $P' = 9.7$ W/cm^2 (black), 5.1 ns at 40P' (purple), 2.4 ns at 100P' (blue), 1.3 ns at 200P' (green), and 812 ps at 400P' (yellow). (b) Defect emission (1.45 eV) obtained with WZ-phase nanoneedle with increasing pump power. The carrier lifetime is 10.5 ns at $P' = 9.7$ W/cm^2 (black), 5.7 ns at 20P' (purple), and 6.0 ns at 100P' (blue). (c) WZ emission (1.49 eV) from WZ-phase nanoneedle with increasing pump power. The carrier lifetime is 314 ps at 40P' (purple), 359 ps at 100P' (blue), 341 ps at 200P' (green), and 345 ps at 600P' (yellow). (d) Comparison of the carrier recombination lifetimes of mixed-phase nanoneedle and WZ-phase nanoneedle for varying pump powers. (e) IQE data (dots) extracted from power-dependent PL measurements at different temperatures, fitted with the Arrhenius equation (curves). Blue plot: mixed-phase nanoneedle, where IQE is 10% at 298 K. Red plot: WZ-phase nanoneedle, where IQE is 25% at 298 K. (f) Comparison of the integrated PL intensities at different pump powers for typical mixed-phase nanoneedle (blue) and WZ-phase nanoneedle (red), at 4 K (solid dots) and 298 K (empty dots). The emission from mixed-phase nanoneedles at room temperature is too weak to be collected below 1×10^3 mW/cm^2 power density (shown by the blue curve with empty dots).

single photon counting (TCSPC) was used to probe the carrier decay rate through the PL emission, by incorporating an avalanche photodiode (APD) into the μ-PL setup. Through calibration with the titanium−sapphire femtosecond laser source, the impulse response of the TRPL setup was derived and found to offer a timing resolution of about 40 ps, with a decay tail of approximately 300 ps due to carrier transition delay inside the APD. When the carrier decay lifetime exceeds one time period of the pulsed laser source (12.5 ns), an electro-optic-modulator based pulse picker was used to reduce the repetition frequency from 80 MHz to 8 MHz, enabling long decay time to be measured more accurately. The mostly-ZB-phase nanoneedles are not included here, because they are from the same sample A and can be represented by mixed-phase nanoneedles in this section.

Figure 4 displays TRPL decay traces under varying pump powers for the mixed-phase nanoneedle (Figure 4a) and the WZ-phase nanoneedle (Figure 4b,c), fitted with exponential decay functions. For mixed-phase nanoneedle, the temporal behavior of the type-II emission peak was studied. Under a very low pump power density of about 9.7 W/cm^2 (defined as P' here), the fitted decay curve yields an extremely long carrier lifetime of 13.5 ns. This can be attributed to the type-II band structure, which induces spatial separation of electrons and holes.[27,28] The carrier lifetime falls as the pump power increases, as can be seen by the purple, blue, green, and yellow lines in Figure 4a.

The detection wavelength for the WZ-phase nanoneedle was varied with increasing pump power from the defect-emission peak at 1.45 eV (Figure 4b) to the WZ-emission peak at 1.49 eV (Figure 4c). Under the same low pump power of P', the defect-emission peak exhibits a long lifetime of 10.5 ns. When pumped at 20P' and 50P', the WZ-emission peak at 1.49 eV emerges and becomes dominant, while the defect-emission peak saturates. This leads to carrier lifetimes of around 6 ns for saturated defect-emission and biexponential behavior caused by an overlap with the WZ-emission peak. This confirms that the defect emission at 1.45 eV, which is the result of impurities or radiative defects, is not sufficiently dominant to confine a large proportion of carriers. Probing at 1.49 eV, the carrier lifetime remains at around 300 ps (Figure 4c) even though the power density increases from 40P' (purple) to 600P' (yellow); this is as a result of the fact that the resolution limit of the timing system has almost been reached.

We note that the TRPL decay curves for both mixed-phase and WZ-phase nanoneedles are single exponential, indicating a lack of nonradiative recombination and dominance of radiative recombination even at very high pump powers.[29,30] The ability to scale up the size of the nanoneedles is beneficial for nanostructure-based optoelectronic devices, as it essentially reduces the surface recombination probability. Meanwhile, the absence of a fast nonradiative recombination portion in the decay curves indicates the superior surface quality of the InP nanoneedles.[31]

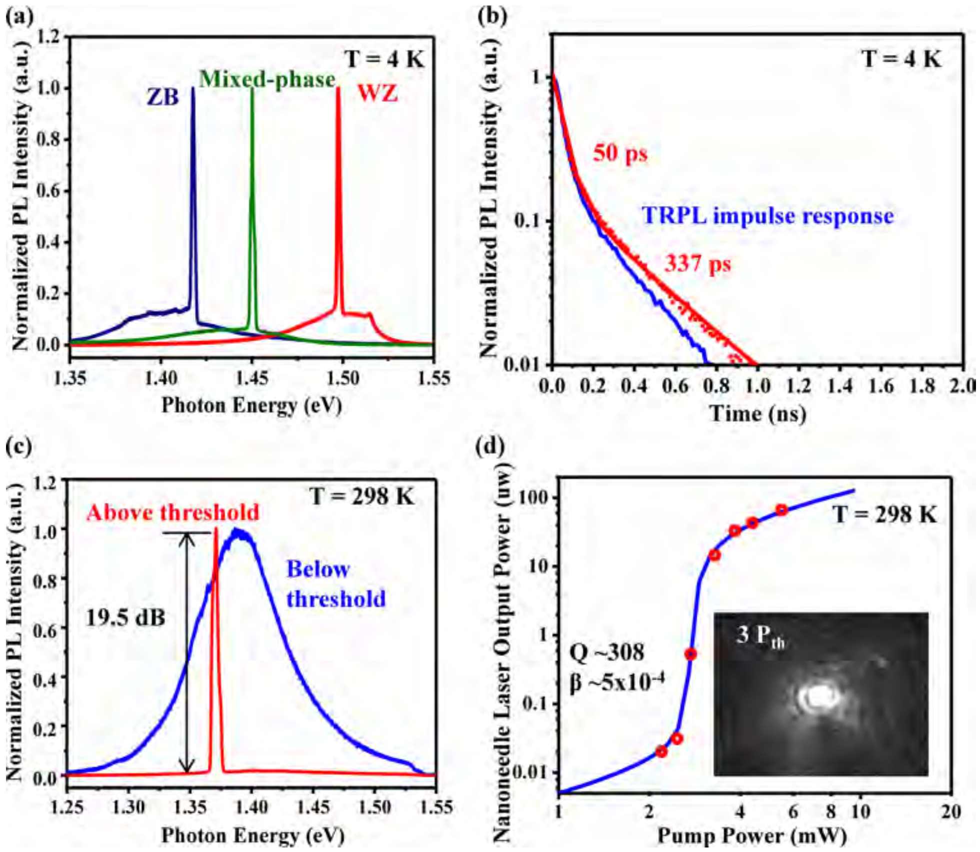

Figure 5. InP nanoneedle lasing. Nanoneedles optically pumped by a titanium−sapphire fs laser at 750 nm. (a) Lasing spectra observed at different photon energies for typical WZ-phase nanoneedles (red), typical mixed-phase naoneedles (green), and mostly-ZB-phase nanoneedles (blue). All PL intensities are normalized for visibility. (b) TRPL decay curves for WZ-phase nanoneedles after lasing (red line). The lifetime falls to approximately 50 ps, and the tail is due to biexponential system impulse response (blue curve, resolution limit 40 ps with 300 ps tail). (c) Typical lasing spectrum of a room-temperature laser, achieved by optically pumping an upright mixed-phase nanoneedle from the top plane. Spectra below (blue) and above (red) lasing threshold are normalized for visibility. A high suppression ratio of 19.5 dB and full-width at half-maximum of 5.5 meV (3.6 nm) is obtained after lasing. (d) Corresponding L−L curve for the nanoneedle laser in c. Analysis reveals a Q of 308 and β of 5×10^{-4}. Both pump power and nanoneedle laser emission are converted into average powers. Inset shows the speckle patterns above the lasing threshold (P_{th}) of 2.7 mW and signifies lasing oscillation.

The carrier lifetimes of mixed-phase nanoneedles and WZ-phase nanoneedles are further compared in Figure 4d. At $10P'$, the carrier recombination speed of pure WZ-phase nanoneedles is around 30 times faster than that of mixed-phase nanoneedles. This indicates that the band-edge recombination of WZ-phase nanostructures offers much higher emission efficiency than the indirect type-II recombination of mixed-phase nanostructures. This difference is underscored when IQE values are obtained through directly comparing the PL intensities pumped by a pulsed laser at different temperatures.[32] Assuming a 100% IQE at 4 K for all nanoneedles pumped to saturated PL intensities, 10% IQE at room temperature (298 K) can be obtained for mixed-phase nanoneedles, while typical WZ-phase nanoneedles offer a more-than-doubled efficiency of around 25% (Figure 4e). A detailed PL intensity comparison is shown in Figure 4f under varying CW-laser pump powers at both 4 K and 298 K. Notably, WZ-phase nanoneedles typically yield a PL intensity more than 3 orders of magnitude larger than that of mixed-phase nanoneedles. With respect to photovoltaic applications, III−V nanostructures offer more efficient light absorption and significant cost reduction, especially when they are grown on silicon substrate.[1] However, nanostructures are known to suffer from undesired nonradiative surface recombinations brought about by a large surface-to-volume ratio. These nonradiative losses can significantly reduce the IQE, resulting in a decrease in the open-circuit voltage (V_{OC}).[33,34] Given their ability to be scaled up to diameters far above the critical dimension, the InP nanoneedles reported here offer an outstanding IQE while still conferring the other advantages of nanostructures for photovoltaics. Furthermore, a larger bandgap can also increase V_{OC},[34] which makes single-crystal WZ-phase InP nanoneedles on silicon stand out as a promising candidate for high-efficiency low-cost photovoltaics.

Each as-grown nanoneedle provides a natural optical cavity, supporting unique helically propagating resonance modes.[7,35] The large size of the nanoneedle ensures that modes are well-confined inside the cavity, leading to very effective gain-mode overlap. Combined together, this enables lasing of single nanoneedle as-grown on silicon, optically pumped by titanium−sapphire femtosecond laser at 750 nm. Figure 5a demonstrates lasing (at 4 K) at different photon energies for the nanoneedles shown in Figure 2a−c, respectively. The close gain-mode matching suggests the potential to tune the lasing wavelength by tailoring the crystal phase and is an area worthy of future exploration. Upon lasing, nanoneedles demonstrate an ultrafast carrier lifetime of around 50 ps (red plot, Figure 5b).[36] The biexponential appearance is due to the fact that the resolution limit of the TRPL timing system, whose impulse response is shown by the blue curve, has been reached.

Room-temperature laser oscillation is demonstrated with InP nanostructures on silicon for the first time, to the best of our knowledge, by optically pumping an upright mixed-phase nanoneedle from the top. The typical spectrum of a room-temperature nanoneedle laser is shown in Figure 5c. A gain model was established, followed by rate equation analysis, in order to fit the corresponding light–light (L–L) curve.[7] The fitted L–L curve in Figure 5d reveals an estimated cavity quality factor (Q) of 308 and a spontaneous emission coupling factor (β) of approximately 5×10^{-4}. When the pump power is below lasing threshold, only a small spot of spontaneous emission could be observed on the camera image. Upon lasing, strong speckle patterns appear (see inset in Figure 5d), which is usually regarded as a classic signature of lasing oscillation. The fact that mixed-phase nanoneedles rather than pure WZ-phase nanoneedles are able to lase at room temperature is somewhat counterintuitive. We attribute this to the influence of the taper angle of the nanoneedle sidewalls on the optical cavity's quality.[7] Sidewall taper is the primary loss mechanism for our as-grown cavities; the smaller taper angle of mixed-phase nanoneedles results in less light leakage through the cavity sidewalls and therefore a better optical cavity. Engineering the taper angle thus offers an avenue to improve future laser performance.

In summary, high-quality InP nanoneedles were grown directly onto a silicon substrate using a low-temperature MOCVD technique. Three types of nanoneedles were explored, composed of ZB/WZ-mixed phase, mostly ZB-phase, and single-crystal WZ-phase, respectively. The optical properties of each category of nanoneedles were studied and linked to the physics of the different underlying band structures. Mixed-phase nanoneedles exhibit type-II emission from 4 to 298 K, with significant blue-shift behavior observed up to 110 K. The spatial separation of carriers leads to an extremely long recombination lifetime of 13.5 ns at 4 K and an IQE of 10% at room temperature. In contrast, pure WZ-phase nanoneedles show a band-edge emission of 1.49 eV at 4 K and 1.41 eV at 298 K, which is approximately 80 meV higher than the bandgap of conventional ZB-phase InP. This more efficient band-edge emission results in a carrier recombination in the pure WZ-phase nanoneedles that is around 30 times faster (300 ps at 4 K) and an IQE that is more than twice as large (25% at 298 K), as compared to the mixed-phase nanoneedles. All three classes of nanoneedles are able to achieve optically pumped lasing at different wavelengths, with an ultrafast lifetime of 50 ps. With higher bandgap and internal quantum efficiency, single-crystal WZ-phase nanoneedles are highly promising nanostructures for use in optoelectronic devices such as photovoltaic cells. In addition, InP nanolasers grown on silicon could form the basis of long-wavelength heterostructure III–V lasers that are compatible with silicon technology.

AUTHOR INFORMATION

Corresponding Author

*E-mail: cch@berkeley.edu.

Author Contributions

K.L. and H.S. contributed equally to this work.

Notes

The authors declare no competing financial interest.

ACKNOWLEDGMENTS

The work was supported by U.S. DOE SunShot Program (contract DE-EE0005316), DoD NSSEFF Fellowship (contract N00244-09-1-0013 and N00244-09-1-0080), California Advanced Solar Technologies Institute, UC Multicampus Research Program and Institute (MRPI), the Center for Energy Efficient Electronics Science (NSF Award 0939514), and the Alexander von Humboldt Research Award. The authors acknowledge W. S. Ko's technical support for figure preparation.

REFERENCES

(1) Borgstrom, M. T.; Wallentin, J.; Heurlin, M.; Falt, S.; Wickert, P.; Leene, J.; Magnusson, M. H.; Deppert, K.; Samuelson, L. Nanowires with promise for photovoltaics. *IEEE J. Sel. Top. Quant. Electron.* **2011**, *17*, 1050–1061.

(2) Mariani, G.; Wong, P. S.; Katzenmeyer, A. M.; Leonard, F.; Shapiro, J.; Huffaker, D. L. Patterned radial GaAs nanopillar solar cells. *Nano Lett.* **2011**, *11*, 2490–2494.

(3) Wallentin, J.; Anttu, N.; Asoli, D.; Huffman, M.; Aberg, I.; Magnusson, M. H.; Siefer, G.; Fuss-Kailuweit, P.; Dimroth, F.; Witzigmann, B.; Xu, H. Q.; Samuelson, L.; Deppert, K.; Borgstrom, M. T. InP nanowire array solar cells achieving 13.8% efficiency by exceeding the ray optics limit. *Science* **2013**, *339*, 1057–1060.

(4) Martensson, T.; Svensson, C. P. T.; Wacaser, B. A.; Larsson, M. W.; Seifert, W.; Deppert, K.; Gustafsson, A.; Wallenberg, L. R.; Samuelson, L. Epitaxial III-V nanowires on silicon. *Nano Lett.* **2004**, *4*, 1987–1990.

(5) Shin, J. C.; Kim, K. H.; Yu, K. J.; Hu, H.; Yin, L.; Ning, C. Z.; Rogers, J. A.; Zuo, J. M.; Li, X. $In_xGa_{1-x}As$ nanowires on silicon: one-dimensional heterogeneous epitaxy, bandgap engineering, and photovoltaics. *Nano Lett.* **2013**, *11*, 4831–4838.

(6) Krogstrup, P.; Jorgensen, H. I.; Heiss, M.; Demichel, O.; Holm, J. V.; Aagesen, M.; Nygard, J.; Morral, A. F. I. Single-nanowire solar cells beyond the Shockley-Queisser limit. *Nat. Photonics* **2013**, *7*, 306–310.

(7) Chen, R.; Tran, T. D.; Ng, K. W.; Ko, W. S.; Chuang, L. C.; Sedgwick, F. G.; Chang-Hasnain, C. Nanolasers grown on silicon. *Nat. Photonics* **2011**, *5*, 170–175.

(8) Lu, F.; Tran, T. D.; Ko, W. S.; Ng, K. W.; Chen, R.; Chang-Hasnain, C. Nanolaser grown on silicon-based MOSFETs. *Opt. Express* **2012**, *20*, 12171–12176.

(9) Chuang, L. C.; Moewe, M.; Chase, C.; Kobayashi, N. P.; Chang-Hasnain, C. Critical diameter for III-V nanowires grown on lattice-mismatched substrates. *Appl. Phys. Lett.* **2007**, *90*, 043115.

(10) Ng, K. W.; Ko, W. S.; Tran, T. D.; Chen, R.; Nazarenko, M. V.; Lu, F.; Dubrovskii, V. G.; Kamp, M.; Forchel, A.; Chang-Hasnain, C. J. Unconventional growth mechanism for monolithic integration of III-V on silicon. *ACS Nano* **2013**, *7*, 100–107.

(11) Chuang, L. C.; Sedgwick, F. G.; Chen, R.; Ko, W. S.; Moewe, M.; Ng, K. W.; Tran, T. D.; Chang-Hasnain, C. GaAs-Based nanoneedle light emitting diode and avalanche photodiode monolithically integrated on a silicon substrate. *Nano Lett.* **2011**, *11*, 385–390.

(12) Chen, R.; Parekh, D.; Ng, K. W.; Chang-Hasnain, C. High-speed avalanche photodiodes using III-V nanopillars monolithically grown on silicon. *IEEE 9th Int. Conf. Group IV Photonics (GFP)* **2012**, 48–50.

(13) Ren, F.; Ng, K. W.; Li, K.; Sun, H.; Chang-Hasnain, C. J. High-quality InP nanoneedles grown on silicon. *Appl. Phys. Lett.* **2013**, *102*, 012115.

(14) Smith, L. M.; Jackson, H. E.; Yarrison-Rice, J. M.; Jagadish, C. Insights into single semiconductor nanowire heterostructures using time-resolved photoluminescence. *Semiconductor Sci. Technol.* **2010**, *25*, 024010.

(15) Murayama, M.; Nakayama, T. Chemical trend of band offsets at wurtzite/zinc-blende heterocrystalline semiconductor interfaces. *Phys. Rev. B* **1994**, *49*, 4710.

(16) Jancu, J. M.; Gauthron, K.; Largeau, L.; Patriarche, G.; Harmand, J. C.; Voisin, P. Type II heterostructures formed by zinc-

blende inclusions in InP and GaAs wurtzite nanowires. *Appl. Phys. Lett.* **2010**, *97*, 041910.

(17) Caroff, P.; Dick, K. A.; Johansson, J.; Messing, M. E.; Deppert, K.; Samuelson, L. Controlled polytypic and twin-plane superlattices in III-V nanowires. *Nat. Nanotechnol.* **2009**, *4*, 50−55.

(18) Ikejiri, K.; Kitauchi, Y.; Tomioka, K.; Motohisa, J.; Fukui, T. Zinc blende and wurtzite crystal phase mixing and transition in indium phosphide nanowires. *Nano Lett.* **2011**, *11*, 4314−4318.

(19) Paiman, S.; Gao, Q.; Joyce, H. J.; Kim, Y.; Tan, H. H.; Jagadish, C.; Zhang, X.; Guo, Y.; Zou, J. Growth temperature and V/III ratio effects on the morphology and crystal structure of InP nanowires. *J. Phys. D: Appl. Phys.* **2010**, *43*, 445402.

(20) Gadret, E. G.; Dias, G. O.; Dacal, L. C. O.; de Lima, M. M., Jr.; Ruffo, C. V. R. S.; Iikawa, F.; Brasil, M. J. S. P.; Chiaramonte, T.; Cotta, M. A.; Tizei, L. H. G.; Ugarte, D.; Cantarero, A. Valence-band splitting energies in wurtzite InP nanowires: Photoluminescence spectroscopy and ab initio calculations. *Phys. Rev. B* **2010**, *82*, 125327.

(21) Miura, K.; Iguchi, Y.; Tsubokura, M.; Kawamura, Y. The growth of high quality GaAsSb and type-II InGaAs/GaAsSb superlattice structure. *J. Appl. Phys.* **2013**, *113*, 143506.

(22) Zhang, L.; Luo, J. W.; Zunger, A.; Akopian, N.; Zwiller, V.; Harmand, J. C. Wide InP nanowires with wurtzite/zincblende superlattice segments are type-II whereas narrower nanowires become Type-I: an atomistic pseudopotential calculation. *Nano Lett.* **2010**, *10*, 4055−4060.

(23) Bao, J.; Bell, D. C.; Capasso, F.; Wagner, J. B.; Martensson, T.; Tragardh, J.; Samuelson, L. Optical properties of rotationally twinned InP nanowire heterostructures. *Nano Lett.* **2008**, *8*, 836−841.

(24) O'Donnel, K. P.; Chen, X. Temperature dependence of semiconductor band gaps. *Appl. Phys. Lett.* **1991**, *58*, 2924−2926.

(25) Kobayashi, Y.; Fukui, M.; Motohisa, J.; Fukui, T. Microphotoluminescence spectroscopy study of high-quality InP nanowires grown by selective-area metalorganic vapor phase epitaxy. *Physica E* **2008**, *40*, 2204−2206.

(26) Mishra, A.; Titova, L. V.; Hoang, T. B.; Jackson, H. E.; Smith, L. M.; Yarrison-Rice, J. M.; Kim, Y.; Joyce, H. J.; Gao, Q.; Tan, H. H.; Jagadish, C. Polarization and temperature dependence of photoluminescence from zincblende and wurtzite InP nanowires. *Appl. Phys. Lett.* **2007**, *91*, 263104.

(27) Akopian, N.; Patriarche, G.; Liu, L.; Harmand, J. C.; Zwiller, V. Crystal phase quantum dots. *Nano Lett.* **2010**, *10*, 1198−1201.

(28) Pemasiri, K.; Montazeri, M.; Gass, R.; Smith, L. M.; Jackson, H. E.; Yarrison-Rice, J.; Paiman, S.; Gao, Q.; Tan, H. H.; Jagadish, C.; Zhang, X.; Zou, J. Carrier dynamics and quantum confinement in type II ZB-WZ InP nanowire homostructures. *Nano Lett.* **2009**, *9*, 648−654.

(29) Reitzenstein, S.; Munch, S.; Hofmann, C.; Forchel, A.; Crankshaw, S.; Chuang, L. C.; Moewe, M.; Chang-Hasnain, C. Time resolved microphotoluminescence studies of single InP nanowires grown by low pressure metal organic chemical vapor deposition. *Appl. Phys. Lett.* **2007**, *91*, 091103.

(30) Chauvin, N.; Alouane, M. H. H.; Anufriev, R.; Khmissi, H.; Naji, K.; Patriarche, G.; Bru-Chevallier, C.; Gendry, M. Growth temperature dependence of exciton lifetime in wurtzite InP nanowires grown on silicon substrate. *Appl. Phys. Lett.* **2012**, *100*, 011906.

(31) Chrankshaw, S.; Reitzenstein, S.; Chuang, L. C.; Moewe, M.; Munch, S.; Bockler, C.; Forchel, A.; Chang-Hasnain, C. Recombination dynamics in wurtzite InP nanowires. *Phys. Rev. B* **2008**, *77*, 235409.

(32) Watanabe, S.; Yamada, N.; Nagashima, M.; Ueki, Y.; Sasaki, C.; Yamada, Y.; Taguchi, T.; Tadatomo, K.; Okagawa, H.; Kudo, H. Internal quantum efficiency of highly-efficient $In_xGa_{1-x}N$-based near-ultraviolet light-emitting diodes. *Appl. Phys. Lett.* **2003**, *83*, 4906.

(33) Ross, R. T. Some thermodynamics of photochemical systems. *J. Chem. Phys.* **1967**, *46*, 4590−4593.

(34) Miller, O.; Yablonovitch, E. Intense internal and external fluorescence as solar cells approach the Shockley-Queisser efficiency limit. *IEEE J. Photovoltaics* **2012**, *2*, 303−311.

(35) Tran, T.; Chen, R.; Ng, K. W.; Ko, W. S.; Lu, F.; Chang-Hasnain, C. J. Helically propagating modes in InGaAs nanoneedle lasers grown on poly-silicon and silicon substrates. *Conf. Lasers Electro-Opt.*, Baltimore, MD, May 1−6, **2011**, CTuR3 (OSA).

(36) Johnson, J. C.; Knutsen, K. P.; Yan, H.; Law, M.; Zhang, Y.; Yang, P.; Saykally, R. J. Ultrafast carrier dynamics in single ZnO nanowire and nanoribbon lasers. *Nano Lett.* **2004**, *4*, 197−204.